L1-norm vs. L2-norm fitting in optimizing focal multi-channel tES stimulation: linear and semidefinite programming vs. weighted least squares

Fernando Galaz Prieto*, Atena Rezaei, Maryam Samavaki, Sampsa Pursiainen

Computing Sciences Unit, Faculty of Information Technology and Communication Sciences, Tampere University, Tampere, Finland

ARTICLE INFO

ABSTRACT

Background and Objective: This study focuses on Multi-Channel Transcranial Electrical Stimulation, a non-invasive brain method for stimulating neuronal activity under the influence of low-intensity currents. We introduce a mathematical formulation for finding a current pattern that optimizes an L1-norm fit between a given focal target distribution and volumetric current density inside the brain. L1-norm is well-known to favor well-localized or sparse distributions compared to L2-norm (least-squares) fitted estimates.

Methods: We present a linear programming approach that performs L1-norm fitting and penalization of the current pattern (L1L1) to control the number of non-zero currents. The optimizer filters a large set of candidate solutions using a two-stage metaheuristic search from a pre-filtered set of candidates.

Results: The numerical simulation results obtained with both 8- and 20-channel electrode montages suggest that our hypothesis on the benefits of L1-norm data fitting is valid. Compared to an L1-norm regularized L2-norm fitting (L1L2) via semidefinite programming and weighted Tikhonov least-squares method (TLS), the L1L1 results were overall preferable for maximizing the focused current density at the target position, and the ratio between focused and nuisance current magnitudes.

Conclusions: We propose the metaheuristic L1L1 optimization approach as a potential technique to obtain a well-localized stimulus with a controllable magnitude at a given target position. L1L1 finds a current pattern with a steep contrast between the anodal and cathodal electrodes while suppressing the nuisance currents in the brain, hence, providing a potential alternative to modulate the effects of the stimulation, e.g., the sensation experienced by the subject.

1. Introduction

In this numerical simulation study, we consider the task of optimizing stimulation currents in the multi-channel version of Transcranial Electrical Stimulation (tES) [1,2] which is non-invasively applied for stimulating neuronal activity, treating psychiatric disorders and studying neuronal behavior. In tES, a current pattern is injected throughout a set of electrode patches attached to the subject's head. Part of the generated diffusive current field penetrates through the skull into the brain, modulating cortical excitability [3]. The procedure for adjusting the electrode montage delivering the stimulus varies from one method to another, considering various properties such as the number of active electrodes, physical description (e.g., positioning, shape, permittivity, and impedance values), applied stimulus waveform (e.g., amplitude, pulse shape, pulse width, and polarity), the number of stimulation sessions, and time interval [4].

This study focuses on Transcranial direct current stimulation (tDCS), one of the non-invasive brain stimulation techniques from the tES family. This method relies on delivering constant, low-intensity currents injections typically ranging from 0.5 to 4.0 mA [5,6] over a pair of large saline-soaked 20–35 cm^2 electrode patches [7], with one patch adhered on the scalp, whereas the second patch can be either cephalic or extra-cephalic [8,9]. The drawback, however, is the limitation of delivering target-specific frequencies and the lack of focality. tDCS is a well-known treatment of neuropsychiatric disorders and brain illnesses, for instance, stroke conditions [5,10], epilepsy syndromes [11], Parkinson's disease [12–15], major depression disorder [16–18], tinnitus [19], migraine [20], and alcoholism [21].

---

* Corresponding author at: Sähkötalo building, Korkeakoulunkatu 3, Tampere, 33720, FI.
E-mail address: fernando.galazprieto@tuni.fi (F. Galaz Prieto).

Multi-channel tES generally constitutes a task of selecting a multi-component current pattern to create a sought field in a given target location. Advanced optimization methods often operate with regularized data fitting strategies to maximize this current [2,22–25]. Determining such a pattern poses an ill-posed inverse problem [26,27], i.e., it does not have a unique solution, and a slight change can significantly change the resulting current density in the brain and can be considered as an over-determined case since the three-dimensional current field is likely to have more degrees of freedom than the current pattern.

This study aims at finding current patterns that would optimize an L1-norm fit between a given focal (well-localized) target current distribution and minimize the dose injected to the subject. To achieve this, we introduce an L1-norm fitted and regularized (L1L1) linear programming approach for finding a focal current distribution since L1-norm based solutions are generally known to be well-localized compared to regularized least squares estimation in inverse modeling [26,27]. We compare the performance of the proposed method against the L1-norm regularized L2-norm fitted (L1L2) semidefinite programming method and the Tikhonov regularized Least Squares (TLS) method [23]. While L1-norm was previously applied to penalize an objective function [24], and linear programming as a strategy to maximize current density at a given location [22], our present method is one of the first to optimize a global L1-norm fit for the tES application.

We consider the present optimization problem as a meta-heuristic task of computational intelligence. The goal is to find the best fitting solution which maximizes both ratio between focused and nuisance current intensity and the amplitude of the focused current density at the targeted stimulus location. The comparison was performed by coupling the CVX optimization toolbox [28] with MATLAB-based Zeffiro Interface (ZI) code package[1] [29–31], which allows creating a lead field matrix [9] for a multi-compartment volume head model (Appendix A.3) using the Finite Element Method (FEM) together with Complete Electrode Model (CEM) [32,33] boundary conditions (Appendix A). As a test domain, we used a realistic head model obtained from an openly available MRI data set (2.5). We hypothesize that our method can be advantageous for a configuration where the focal current distribution is sought using a limited number of electrodes to deliver the stimulus.

This article is structured as follows: The methodological details, including optimization techniques, two-stage metaheuristic search, test domain, and target placement, are described in Section 2. The results can be found in Section 3 and discussion in Section 4. The mathematical grounds and principles of tES forward modeling and weighted least squares are explained in Appendices A.1 and Appendix B.

2. Methods

The inverse problem of tES is to find a current pattern $\mathbf{y} = (y_1, y_2, \ldots, y_\ell)$ that can generate a given current field which in the discretized form can be expressed as a coordinate vector $\hat{\mathbf{x}} = (\hat{x}_1, \hat{x}_2, \ldots, \hat{x}_N)$. The fitting between vectors $\mathbf{y}$ and $\hat{\mathbf{x}}$ is enabled by the matrix equation

$$\hat{\mathbf{L}}\mathbf{y} = \hat{\mathbf{x}}, \tag{1}$$

where $\hat{\mathbf{L}}$ is a linear mapping following discretized Maxwell's equations (Appendix A.1). We consider finding an optimized current pattern which, when this is applied to the head model $\mathbf{\Omega}$ through a given number of active electrodes attached to the scalp, generates a focused volume current distribution matching a synthetic dipolar

current at a given orientation and location while the nuisance field component remains suppressed.

The sought current pattern is required to meet Kirchhoff's current conservation conditions, i.e., the total sum of injected currents must be equal to zero, $\sum_{\ell=1}^{L} y_\ell = 0$. Such conditions can be rewritten as $\mathbf{1}^T\mathbf{y} = 0$ with $\mathbf{1} = (1, 1, \ldots, 1)^T$ to yield both a total dose $\|\mathbf{y}\|_1 = \sum_{\ell=1}^{L} |y_\ell|$ less or equal to a given safety current limit μ, and an entry-wise upper limit of less or equal to γ, i.e., $\mathbf{y} \preceq \gamma\mathbf{1}$. The maximum absolute total dose can be achieved with a montage of at least a minimum set of two electrodes (one bearing positive polarity and the other one negative) [5,6]. For an even comparison between different optimized current patterns, the total dose of each pattern is equaled to $\mu = 4.0$ mA. We can assume that the highest current an electrode can bear is $\gamma = 2.0$ mA [6].

2.1. Optimization

We consider a weighted optimization scheme [23] to solve

$$\mathbf{L}\mathbf{y} = \mathbf{x}, \tag{2}$$

where $\quad \mathbf{L} = \begin{pmatrix} \mathbf{L}_1 \\ \mathbf{L}_2 \end{pmatrix} = \begin{pmatrix} \mathbf{P}\hat{\mathbf{L}}_1 \\ \hat{\mathbf{L}}_2 \end{pmatrix}, \quad \mathbf{x} = \begin{pmatrix} \mathbf{x}_1 \\ \mathbf{0} \end{pmatrix} = \begin{pmatrix} \mathbf{P}\hat{\mathbf{x}}_1 \\ \mathbf{0} \end{pmatrix}.$

Here, $\hat{\mathbf{L}}_1$, $\hat{\mathbf{L}}_2$, and $\hat{\mathbf{x}}_1$ are obtained by splitting $\hat{\mathbf{L}}$ and $\hat{\mathbf{x}}$ into two different components

$$\hat{\mathbf{L}} = \begin{pmatrix} \hat{\mathbf{L}}_1 \\ \hat{\mathbf{L}}_2 \end{pmatrix} \quad \text{and} \quad \hat{\mathbf{x}} = \begin{pmatrix} \hat{\mathbf{x}}_1 \\ \mathbf{0} \end{pmatrix} \tag{3}$$

and $\mathbf{P}$ represents a matrix that projects a vector into the direction of $\hat{\mathbf{x}}_1$. Because this field has a single direction, the projection can be considered sufficient to measure the match between the focused and the target fields.

We call the first solution component, $\mathbf{L}_1\mathbf{y}$, the *focused field*, i.e., the part that contains the given stimulus target field $\mathbf{x}_1$, and the second one, $\mathbf{L}_2\mathbf{y}$, the *nuisance field*, i.e., the remaining part of the field which we aim to suppress. The amplitude $\|\mathbf{x}_1\|_2$ of the target refers to the value 3.85 A/m^2 (Ampere per square meter), which represents a rough approximate threshold for the excitation of nerve fibers. According to Kowalski et al. [34], the threshold values for the upper limb area of the motor cortex range between 6 and 2.5 A/m^2 at 2.44 kHz (kilohertz) and 50 Hz (hertz). This value is obtained by dividing the average density activity of 0.77 nAm/mm^2 (nano ampere per square millimeter) [35] by the length of a pyramidal cell approximately of 0.2 mm (millimeter) [36] from the apical to the basal dendrites. It is roughly one magnitude greater than the achievable focused current density in the brain [9] given the safety limitations of tES. Here, it is considered a reference amplitude to normalize the present optimization framework.

The magnitude difference between $\mathbf{L}_1\mathbf{y}$ and $\mathbf{L}_2\mathbf{y}$ can be controlled by varying the weight of the nuisance field explicitly given for L1L1 and L1L2, and as a penalty parameter embedded in the objective function for TLS, where explicit constraints are not applicable. To limit the number of non-zero currents in $\mathbf{y}$, the objective function of the optimization task is regularized (penalized) by the norm of the current pattern.

2.1.1. L1-norm regularized L1-norm fitting
The following L1-norm regularized L1-norm fitting problem (L1L1) is defined as

$$\min_{\mathbf{y}} \left\{ \left\| \begin{pmatrix} \mathbf{L}_1\mathbf{y} - \mathbf{x}_1 \\ \Psi_\varepsilon[\nu^{-1}\mathbf{L}_2\mathbf{y}] \end{pmatrix} \right\|_1 + \alpha\zeta\|\mathbf{y}\|_1 \right\}, \tag{4}$$

subject to $\mathbf{y} \preceq \gamma\mathbf{1}$, $\|\mathbf{y}\|_1 \leq \mu$, and $\sum_{\ell=1}^{L} y_\ell = 0$. Here, α is the regularization parameter, the scaling factors are $\zeta = \|\mathbf{L}\|_1$ and $\nu =$

$\|\mathbf{x}\|_\infty$, and the mth component of the vector-valued threshold function Ψ_ε has the following form

$$\Psi_\varepsilon[\mathbf{w}]_m = \max\{\,|w_m|, \varepsilon\,\} \quad \text{for} \quad m = 1, 2, \ldots, M, \tag{5}$$

where $\mathbf{w} = (w_1, w_2, \ldots, w_M)$ and $0 \le \varepsilon \le 1$ are the threshold weights. Entries $(\mathbf{L}_2\mathbf{y})_m$ with an absolute value below $\varepsilon\nu$ do not actively contribute to the minimization process due to the threshold. We refer the set $\{\,m : |(\mathbf{L}_2\mathbf{y})_m| \ge \varepsilon\nu\,\}$ as the *constraint support*, i.e., the index set contributing to the value of the objective function.

The choice $\varepsilon = 1$ is equivalent to replacing the minimization aspect from (4) with only $\|\mathbf{L}_1\mathbf{y} - \mathbf{x}_1\|_1 + \alpha\zeta\|\mathbf{y}\|_1$. We consider a positive threshold essential from the numerical point of view. Without it, should $\varepsilon = 0$, the objective function in (4) is equal to $\|\mathbf{x}_1\|_1$, constituting $\mathbf{x} = \mathbf{0}$ a potential global minimizer i.e., a solution that vanishes everywhere.

Problem (4) constitutes the following linear programming task [37, 294]

$$\min_{\mathbf{y}, \mathbf{t}^{(1)}, \mathbf{t}^{(2)}, \mathbf{t}^{(3)}} \left(\sum_{k=1}^{N} t_k^{(1)} + \sum_{m=1}^{M} t_m^{(2)} + \alpha\zeta \sum_{\ell=1}^{L} t_\ell^{(3)} \right) \tag{6}$$

subject to

$$-\begin{pmatrix} \mathbf{t}^{(1)} \\ \mathbf{t}^{(2)} \\ \alpha\zeta\mathbf{t}^{(3)} \end{pmatrix} \preceq \begin{pmatrix} \mathbf{L}_1 \\ \mathbf{L}_2 \\ \mathbf{I} \end{pmatrix}\mathbf{y} - \begin{pmatrix} \mathbf{x}_1 \\ \mathbf{0} \\ \mathbf{0} \end{pmatrix} \preceq \begin{pmatrix} \mathbf{t}^{(1)} \\ \mathbf{t}^{(2)} \\ \alpha\zeta\mathbf{t}^{(3)} \end{pmatrix},$$

$$\begin{pmatrix} \mathbf{0} \\ \varepsilon\nu\mathbf{1} \end{pmatrix} \preceq \begin{pmatrix} \mathbf{t}^{(1)} \\ \mathbf{t}^{(2)} \end{pmatrix}$$

$$\begin{pmatrix} \mathbf{0} \\ \mathbf{0} \end{pmatrix} \preceq \begin{pmatrix} \mathbf{t}^{(3)} \\ \mathbf{1}^T\mathbf{t}^{(3)} \end{pmatrix} \preceq \begin{pmatrix} \gamma\mathbf{1} \\ \mu \end{pmatrix}$$

$$\mathbf{1}^T\mathbf{y} = 0. \tag{7}$$

Here, $\mathbf{t}^{(1)}$, $\mathbf{t}^{(2)}$ and $\mathbf{t}^{(3)}$ constitute auxiliary N-by-1, M-by-1 and L-by-1 vectors, respectively. A numerically implementable form of (7) with one inequality and equality constraint can be expressed as follows:

$$\min_{\mathbf{y}, \mathbf{t}^{(1)}, \mathbf{t}^{(2)}, \mathbf{t}^{(3)}} \begin{pmatrix} \mathbf{0} \\ \mathbf{1} \\ \mathbf{1} \\ \mathbf{1} \end{pmatrix}^T \begin{pmatrix} \mathbf{y} \\ \mathbf{t}^{(1)} \\ \mathbf{t}^{(2)} \\ \mathbf{t}^{(3)} \end{pmatrix} \tag{8}$$

subject to

$$\begin{pmatrix} \mathbf{L}_1 & -\mathbf{I} & \mathbf{0} & \mathbf{0} \\ \mathbf{L}_2 & \mathbf{0} & -\mathbf{I} & \mathbf{0} \\ -\mathbf{I} & \mathbf{0} & \mathbf{0} & -\mathbf{I} \\ -\mathbf{L}_1 & -\mathbf{I} & \mathbf{0} & \mathbf{0} \\ -\mathbf{L}_2 & \mathbf{0} & -\mathbf{I} & \mathbf{0} \\ \mathbf{I} & \mathbf{0} & \mathbf{0} & -\mathbf{I} \\ \mathbf{0} & -\mathbf{I} & \mathbf{0} & \mathbf{0} \\ \mathbf{0} & \mathbf{0} & -\mathbf{I} & \mathbf{0} \\ \mathbf{0} & \mathbf{0} & \mathbf{0} & -\mathbf{I} \\ \mathbf{0} & \mathbf{0} & \mathbf{0} & \mathbf{I} \\ \mathbf{0} & \mathbf{0} & \mathbf{0} & \mathbf{1}^T \end{pmatrix} \begin{pmatrix} \mathbf{y} \\ \mathbf{t}^{(1)} \\ \mathbf{t}^{(2)} \\ \mathbf{t}^{(3)} \end{pmatrix} \preceq \begin{pmatrix} \mathbf{x}_1 \\ \mathbf{0} \\ \mathbf{0} \\ -\mathbf{x}_1 \\ \mathbf{0} \\ \mathbf{0} \\ \mathbf{0} \\ -\varepsilon\nu\mathbf{1} \\ \mathbf{0} \\ \gamma\mathbf{1} \\ \mu \end{pmatrix} \tag{9}$$

$$\mathbf{1}^T\mathbf{y} = 0. \tag{9}$$

The solution is found via primal-dual interior-point algorithm [37,38] of the SDPT3 package, accessible via the open CVX toolbox[2] [28].

2.1.2. L1-norm regularized L2-norm fitting

The L1-norm regularized L2-norm fitting method (L1L2) is of the form

$$\min_{\mathbf{y}} \left\{ \left\| \begin{pmatrix} \mathbf{L}_1\mathbf{y} - \mathbf{x}_1 \\ \Psi_\varepsilon\left[\nu^{-1}\mathbf{L}_2\mathbf{y}\right] \end{pmatrix} \right\|_2 + \alpha\zeta\|\mathbf{y}\|_1 \right\}, \tag{10}$$

where the L1-norm fitting in (4) is substituted with L2-norm. Notice that if $\varepsilon = 1$, i.e., nuisance field is unconstrained, and a single target is being used, as in this study, then the objective function of both L1L1 and L1L2 is reduced to $\min_{\mathbf{y}}\{|\mathbf{L}_1\mathbf{y} - \mathbf{x}_1| + \alpha\zeta\|\mathbf{y}\|_1\}$. In CVX, the solutions are obtained through semidefinite programming incorporating linear and quadratic constraints. The latter follows the L2-norm fitting straightforwardly [38].

2.1.3. Tikhonov regularized least squares

In Tikhonov regularized least squares (TLS) estimation [22,23], the optimization problem is

$$\min_{\mathbf{y}}\{\|\mathbf{L}_1\mathbf{y} - \mathbf{x}_1\|_2^2 + \alpha^2\delta^2\|\mathbf{L}_2\mathbf{y}\|_2^2 + \alpha^2\varsigma^2\|\mathbf{y}\|_2^2\}, \tag{11}$$

where $\varsigma = \|\mathbf{L}\|_2$. To enforce focality, the nuisance field weight $\delta \ge 0$ is considered as a variable parameter, and the solution of (11) is given by the linear system

$$\left(\mathbf{L}_1^T\mathbf{L}_1 + \alpha^2\delta^2\mathbf{L}_2^T\mathbf{L}_2 + \alpha^2\varsigma^2\mathbf{I}\right)\mathbf{y} = \mathbf{L}_1^T\mathbf{x}_1, \tag{12}$$

which in Matlab can be solved using the *backslash* operator (\) in a straightforward manner. The weight can be shown (Appendix B) to affect the focused current density Γ (A/m²) which is defined as

$$\Gamma = \frac{\mathbf{x}_1^T\mathbf{L}_1\mathbf{y}}{\|\mathbf{x}_1\|_2}, \tag{13}$$

and the current ratio Θ (unitless) which is obtained by

$$\Theta = \frac{\Gamma}{\|\mathbf{L}_2\mathbf{y}\|_2/\sqrt{M}}. \tag{14}$$

While the equations above are dependent on the regularization parameter and the nuisance field weight, the latter is treated differently in each method: as an explicit threshold in the L1L1 and L1L2 methods and as a weighted form for the TLS method leading towards a different solution dependence. When $\delta > 0$, the minimization problem (11) can be re-written as

$$\min_{\mathbf{y}}\{\kappa\|\mathbf{L}_1\mathbf{y} - \mathbf{x}_1\|_2^2 + \|\mathbf{L}_2\mathbf{y}\|_2^2 + \frac{\varsigma^2}{\delta^2}\|\mathbf{y}\|_2^2\} \tag{15}$$

with $\kappa = 1/(\alpha^2\delta^2)$. Thus, either focused or nuisance fields can be weighted.

2.2. Candidate solution set

Determining optimal case-wise parameter combinations is done by analyzing a two-dimensional 15×15 lattice resolution of feasible solutions covering a wide dynamical range with good numerical performance while ensuring a reasonable computation time. In L1L1 and L1L2, α varies between -100 and -30 dB and ε between -160 and 0 dB. In TLS, α is between -200 and -110 dB and δ between -50 and 40 dB.

We computed the solutions on a Dell 5820 workstation with an Intel Core i9-10900X processor and 256GB RAM. The total computing time required to evaluate the entire lattice of candidate solutions was approximately 378, 456, and 20 s with L1L1, L1L2, and TLS, respectively. The L1L1 and L1L2 solutions were parallelized through ten processor threads, while the TLS solutions were simplified by leveraging Matlab's interpreter in a simple iteration utilizing a full system matrix. We used a relative solver tolerance of 1E-12 as a stopping criterion for L1L1 and L1L2.

2.3. Two-stage metaheuristic search

We apply a two-stage metaheuristic lattice search algorithm [39] which finds a set of candidate solutions to optimize the current distribution, given a focal vector field where focused current density Γ and current ratio Θ as metacriteria. Of the following two cases, (A) utilizes both criteria while (B) constitutes a reference for maximizing Γ. In other tES publications, such as [2,3,6,22], Γ and Θ are referred to as *intensity* and *focality*, respectively.

2.3.1. Case (A)

The first stage sets a threshold condition for Γ, and the second stage maximizes the threshold set of candidates concerning Θ. Using these two criteria, the selected candidate will have an adequate current amplitude [25] in the targeted position and a suitably suppressed nuisance field component. To evaluate the overall numerical solver performance, we use the threshold condition 0.11 A/m² and, in addition, show how the optimum behaves as a function of the threshold condition.

2.3.2. Case (B)

For comparison, Case B is a simpler scheme. It considers maximizing only the focused current density Γ over the entire set of candidates, i.e., only a single criterion and stage.

2.3.3. Post-optimization with non-fixed vs. fixed montage

During the first stage of the lattice search, we apply a montage of 128 electrodes, while the second run uses a limited set. The optimizer initially permits all channels during the first stage; however, it only allows those electrodes that contribute the most to the total maximum current value to carry non-zero amplitudes. The rest of the electrodes are then opt-out (set to zero) from further calculations. Thus, only 20 or 8 active channels are available in the montage. The montages are inspired by commercial state-of-the-art tES systems [40,41].

In TLS, the second-stage solution needs to be scaled to match the maximum possible total dose since the least squares optimization process does not automatically yield such scaling, unlike the L1L1 and L1L2 convex optimization techniques.

2.4. Synthetic sources and placement

A total of three dipoles are placed in the following three left hemispheric Brodmann's areas [42]: postcentral gyrus (red), superior temporal gyrus (cyan), and occipital lobe (blue) (Fig. 1a). Each of these dipoles is oriented regarding the surface of the gray matter tissue to satisfy the normal constraint of the brain activity in the cerebral cortex [43]. The amplitude of the dipolar target current is related to the corresponding local current density in the brain. Each current pattern obtained is a solution to the optimization problem corresponding to each one of these areas. The results are categorized as *Somatosensory* for postcentral gyrus, *Auditory* for superior temporal gyrus, and *Visual* for occipital lobe.

2.5. Test domain

As a test domain for the numerical experiments, we used a multi-compartment volume conductor head model based on openly available anatomical T1-weighted Magnetic Resonance Imaging (MRI) data[3] obtained from a real subject. The data were segmented using FreeSurfer Software Suite[4] which distinguishes different head and brain tissue compartments including the scalp,

---

(a) Gray matter and the highlighted regions of interest.
(b) Volume current distribution among the white matter through a five-channel electrode montage.
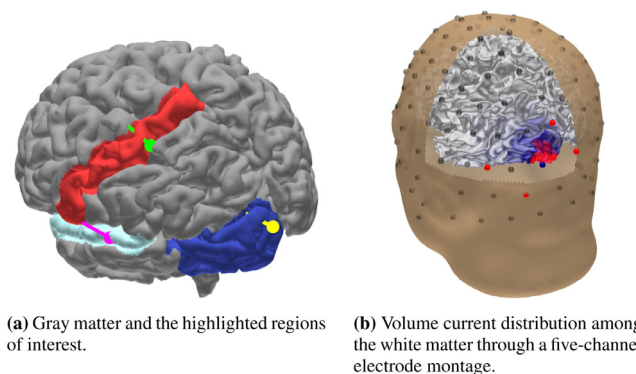
Fig. 1. (a): Left-posterior view of the gray matter compartment of the volume conductor model highlighting the *somatosensory* (red), *auditory* (cyan) and *visual* (blue) region of interest (postcentral gyrus, superior temporal gyrus and occipital lobe in the 36-label Desikan-Killiany atlas). Each region is presented with its own point-like dipolar target current (sphere) and orientation (line). **(b):** An example of a simple five-channel electrode montage creating a volume current distribution in the left-hemisphere of the occipital lobe. The positive (anodal) electrode channels injecting the current into the domain are illustrated with red spheres, the negative (cathodal) ones with blue, and the disabled/inactive ones with dark gray. (For interpretation of the references to colour in this figure legend, the reader is referred to the web version of this article.)

skull, cerebrospinal fluid, gray and white matter, subcortical structures such as brain stem, thalamus, amygdala, and ventricles with their complex geometrical properties [44].

By using Zeffiro Interface (ZI) Finite Element (FE) mesh generator [29], volume segmentation is obtained by identifying the obtained compartments from the surface segmentation and creating smoothed and optimized FE meshes of these compartments. To discretize the head model, we use a FE mesh resolution of 1 mm to obtain physiologically accurate results [45]. The conductivity distribution, which influences the accuracy of the forward solution [46], is constant in each tissue compartment with the values corresponding to the set proposed in [47]. The 128 electrodes are set (Fig. 1b) following International 10-10 electroencephalographic (EEG) hardware system [48] with electrode impedance of 2 kOhm (Kiloohms) uniformly. Impedance modeling was enabled by incorporating CEM into the forward simulation (Appendix A.1). The tES lead field matrix **L** generation is explained in (Appendix A.3) for 1000 uniformly distributed spatial sets of points contained by the gray matter compartment, including three Cartesian degrees of freedom per point.

2.5.1. Performance analysis

The optimization outcome was examined by evaluating focused current density Γ, current ratio Θ, maximum injected current pattern $\|\mathbf{y}\|_\infty$, and the Angle Difference (AD) as

$$\text{AD}(\vec{j_1}, \vec{j_2}) = \arccos\left(\frac{\langle \vec{j_1}, \vec{j_2} \rangle}{\|\vec{j_1}\| \|\vec{j_2}\|}\right), \qquad (16)$$

between the focused and the targeted fields. Here, $\vec{j_1}$ represents volume current distribution at the target location generated by the injected pattern and $\vec{j_2}$ the dipolar target current.

The limits for the lattice-induced deviation of Γ, Θ, AD, and $\|\mathbf{y}\|_\infty$ were estimated by forming a second order Taylor's polynomial approximation over a 3-by-3 subset of the optimization lattice centered at the selected candidate solution using the three-point difference formula [49] to approximate the derivatives and maximizing the deviation in a co-centered square with edge-length matching the lattice size. With this strategy, the deviation is obtained with respect to an hypothetical lattice with double the resolution compared to the actual one.
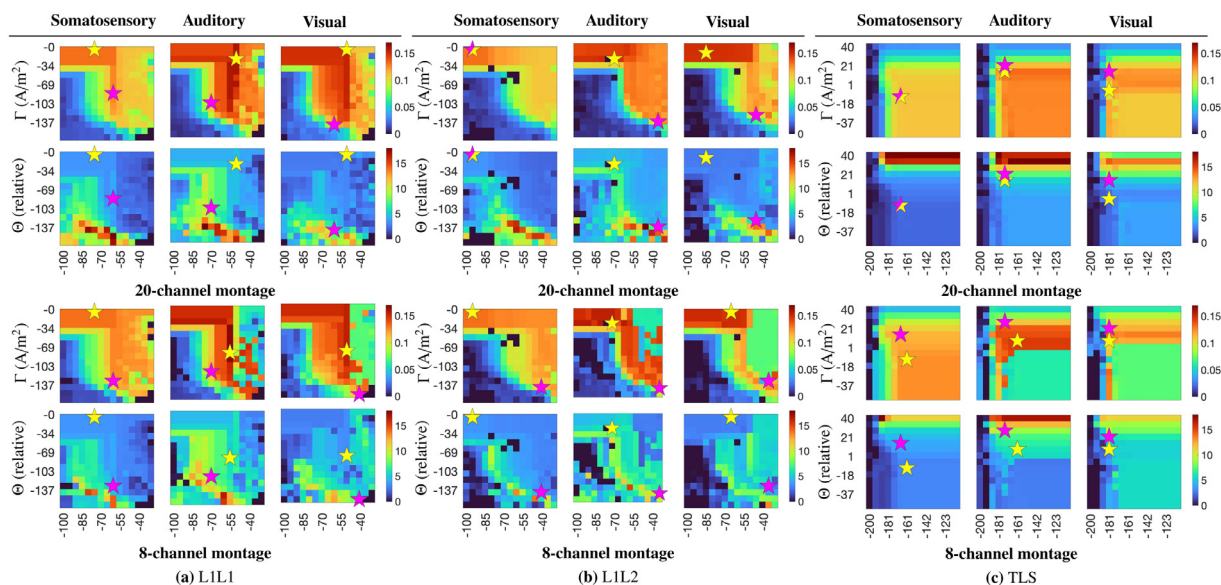
Fig. 2. Γ (A/m^2) and Θ (relative) for each point of the search lattice in the first run of the two-stage metaheuristic optimization process. Horizontal axis corresponds to the regularization parameter α and the vertical axis to the nuisance field weight which is given by ε for L1L1 and L1L2 and δ for TLS. The first-stage optimal solution for the cases (A) and (B) are represented by a purple and yellow star, respectively. The axes are scaled in decibel (dB) units. (For interpretation of the references to colour in this figure legend, the reader is referred to the web version of this article.)

3. Results

Figure 2 illustrates the metaheuristic lattice search outcome. The performance of the optimization methods, including their maximal estimated lattice-induced deviations, are visualized in Figs. 3 and 4. Optimized current patterns (as well as their projections in the brain) for both 20 and 8 channel montage are shown in Figs. 5 and 6, respectively.

3.1. Lattice search interpretation

For each optimization method, the range of the metaheuristic lattice search was sufficient to cover the regions in which Γ was saturated close to its maximum. These regions were surrounded by comparably smooth transition zones, from high to low Γ and with elevated Θ-values. The solutions for cases (A) and (B) were generally found from these saturated and transition regions, respectively. Figure 2a–c show the first-stage optimizers found in the case (A), where Θ is maximized using the threshold $\Gamma \geq 0.11$ A/m^2 (purple star), and in case (B), which finds the global maximizer of Γ (yellow star). The lattice search was found to perform analogously for the 20 and 8 channel montages, which can be observed from the overall small mutual differences between the star points.

Considering L1L1 (Fig. 2a) and L1L2 (Fig. 2b), with regularization parameter α range below -70 dB, Γ is close to its maximum in a region where the nuisance field weight ε is close to 0 dB, i.e., when the optimizer is almost completely determined by the focused field component. In this α-range, the transition towards a greater ratio Θ takes place when ε decreases from -30 to -40 dB (between 0.04 and 0.12 A/m^2), while Γ vanishes with a slightly smaller ε. The α-range between -70 and -40 dB constitutes a *'sweet spot'* (a combination of factors resulting in a maximum response), where Γ is saturated for ε-values down to -150 dB (1E-07 A/m^2). The greatest Θ-values are found near the lower end of this range below which Γ decays to zero. Both Γ and Θ begin to diminish when α reaches a value greater than -40 dB. For TLS (Fig. 2c), when $\alpha \geq -180$ dB, the maximum Γ can be obtained close to 0 dB with Θ growing along with ε. While the value of α can be ob-

served to affect the best obtainable Θ, there is no special range where the dependence of Θ on the ϵ-value would change significantly.

3.2. Optimizer characteristics

In comparison to L1L2 and TLS (Fig. 3), L1L1 yielded greater or equal values of Θ and Γ in cases (A) and (B), respectively. L1L1 tended towards a higher maximum current $\|\mathbf{y}\|_\infty$ and AD than in the cases of L1L2 and TLS. The observed extra gain provided by L1L1, compared to L1L2, was systematic and most pronounced in case (A), and the optimized Θ-value of L1L1 was approximately 1.4 times greater than L1L2 at the first stage of search threshold with Γ set at 0.11 A/m^2, agreeing with our initial hypothesis. Higher threshold levels, exemplified in Fig. 4, can further emphasize this gain up to a factor of 2.

In case (B), the greatest difference between the L1L1- and TLS-optimized focal current density Γ was obtained for the auditory target current with both 8- and 20-channel montages (0.027 and 0.022 A/m^2, respectively). Comparing the results obtained with the 8- and 20-electrode montage, the former one was observed to result in smaller overall differences between the methods and a marginally greater focused current density in case (B).

3.3. Current pattern and volume density

Based on the results, the dependence of the optimization accuracy on the spatial position and orientation of the target dipole becomes evident, while the current patterns obtained via each applied method maintain their general characteristics regardless of the positioning of the target dipole.

L1L1 and L1L2 tend to find a pattern with a greater maximum current of $\|\mathbf{y}\|_\infty$ where the amplitudes have smoother transitions between the electrodes than TLS. However, they also include multiple low-amplitude currents with close-to-equal amplitudes, which distributes the nuisance current over a large area, decreasing its amplitude. This effect can be observed on the 20-channel montage in Fig. 5 and less pronounced in the 8-channel montage 6. Furthermore, the distance between anodal and cathodal electrodes tend to
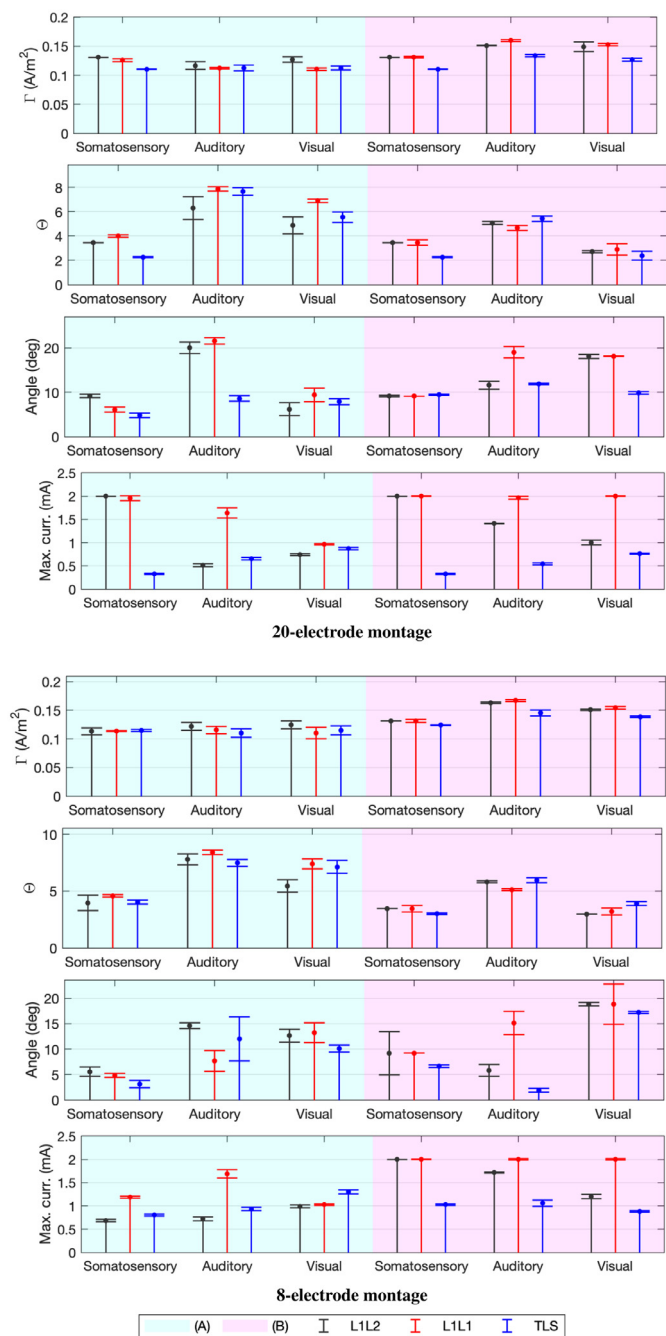
Fig. 3. A graphical illustration optimized values of Γ (A/m^2), Θ (relative), AD (deg), and $\|\mathbf{y}\|_\infty$ (mA) and their maximal estimated lattice-induced deviations. In each case, the dot on the stem shows the optimizer while the whiskers illustrate the estimated limits for the deviation. L1L1 correspond to red while the L1L2 and TLS results in black and blue stems, respectively. The optimization cases (A) and (B) are highlighted with cyan and magenta background color, respectively. (For interpretation of the references to colour in this figure legend, the reader is referred to the web version of this article.)
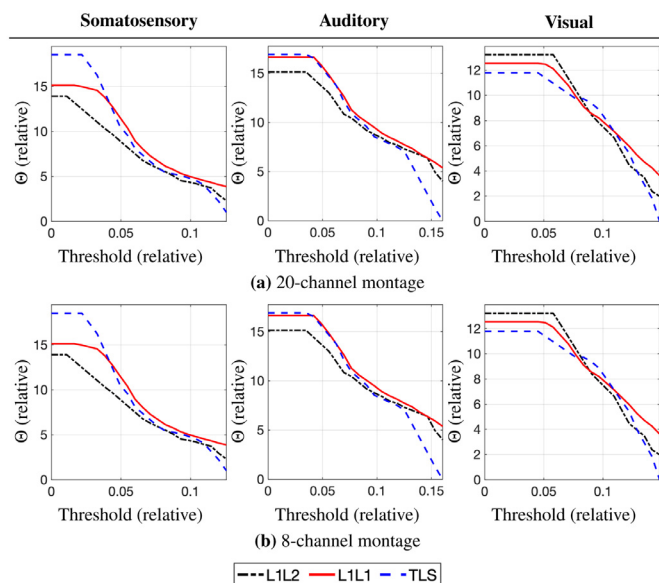

Fig. 4. Current ratio Θ as a function of the threshold condition setting the criterion $\Gamma \geq$ threshold in the first stage of the metaheuristic search. When threshold ≥ 0.11, L1L1 (solid red curve) yields a greater or equal current ratio Θ compared to L1L2 (dash-dotted black curve) and TLS (dashed blue curve). (For interpretation of the references to colour in this figure legend, the reader is referred to the web version of this article.)

4. Discussion

This study considered L1-norm data fitting via L1-norm regularized convex optimization (L1L1) as a potential alternative strategy for finding a current pattern in a multi-channel Transcranial Electrical Stimulation (tES) stimulation. L1-norm is a well-known measurement procedure to yield sparse solutions compared to L2-norm [24,25]. In tES, this means greater focused current density driven in the targeted region of interest. Earlier strategies resorted to this approach for maximizing injected current pattern supplied by a limited number of electrodes patches attached to the scalp of the subject [2,22].

In this study, we applied the L1-norm in both fitting and regularization aspects, i.e., penalization of non-zero entries in the current pattern, hypothesizing that both the resulting volume current distribution and current pattern are sparse. Additionally, our results are compared with L1-regularized L2-norm data fitting (L1L2) [24], and the weighted Tikhonov regularized Least Squares method (TLS) [23].

We consider our data fitting approach advantageous for convex optimization to obtain the best possible fit for a given, user-defined number of active electrodes, from a montage with a minimal set of two channel setting [5,6] to an extended hardware featuring 64, 128 or 256 channels [2]. Here, we applied montages of 20 and 8 active channels inspired by commercial clinically-applied tES systems [40,41].

Our approach can approximate the best regularized and constrained L1/L2-norm fit. A widely adopted approach is to maximize the focused current density with different constraints, e.g., a focality-enforcing upper limit [2,24] for the amplitude of the nuisance current. However, focality not only follows a constraint, but also an objective function. For this reason, L1-norm data fitting seems a potential alternative for finding current patterns, absent in the earlier studies.

The application of metaheuristics conditions allowed selecting problem parameters in such regard that the expected outcome was close-to-optimal concerning a given metacriterion. One can provide
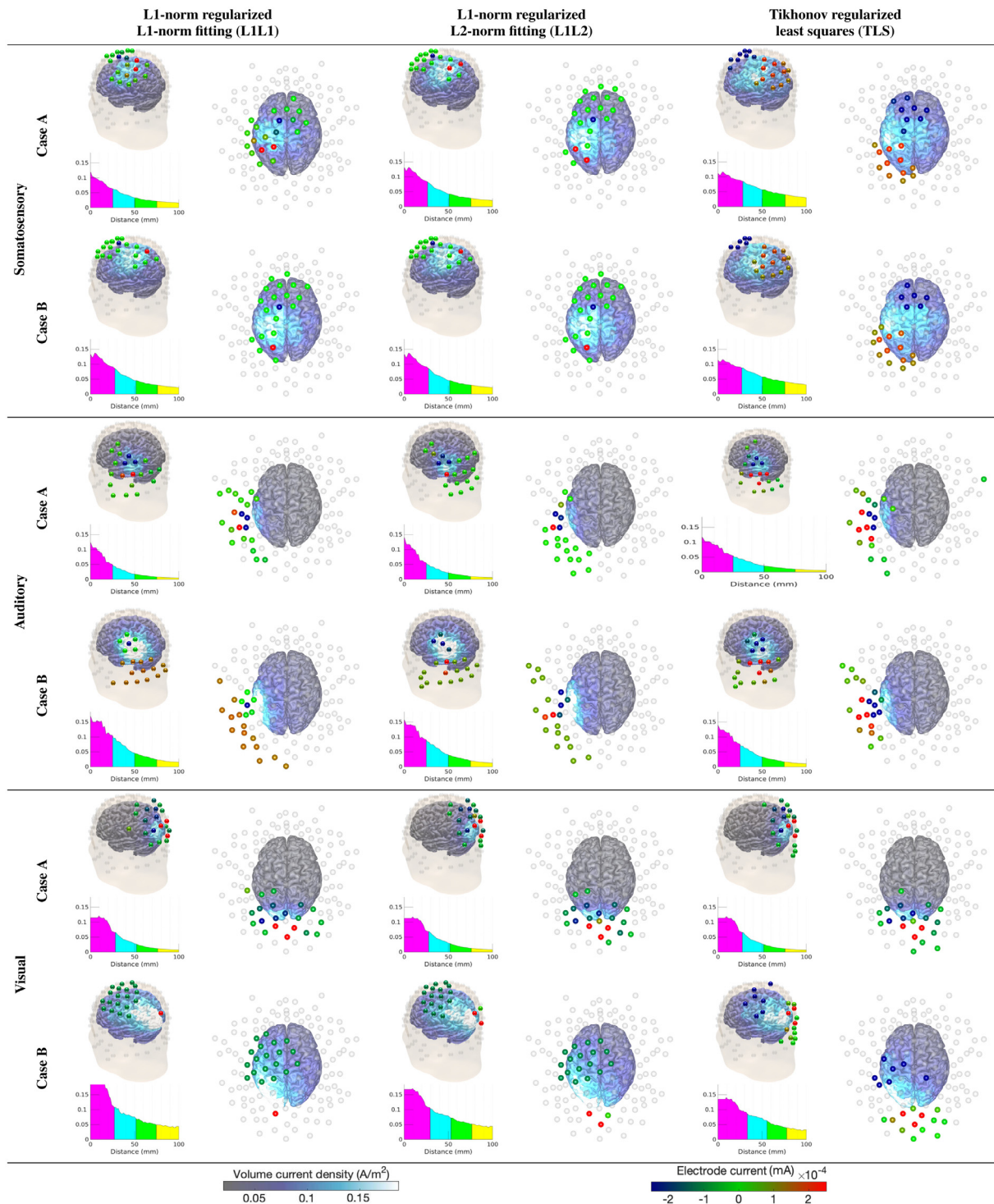
be further apart in L1L1 and L1L2 than in TLS, where distance was minimal, especially in the pattern obtained via optimization strategy (B).

L1L1 seems to find the greatest focal current density with a comparably larger threshold for Γ, allowing for a focal stimulus with a relatively high current density, reflected by the results obtained via optimization strategy (A), where the current ratio Θ was greater for L1L1 than for L1L2 or TLS.

Fig. 5. The 20-channel electrode montage and current pattern (mA) together with corresponding volume current density A/m² were obtained through two consecutive runs of the two-stage metaheuristic optimization process concerning non-fixed and fixed montage of 20 active electrodes, respectively. Average amplitude in the direction of the target dipole is shown as a function of distance (mm) from the dipole position. The current pattern colorbar shows a color gradient interval from -0.25 to 0.25 mA to enhance the visibility of small variations in the pattern. (For interpretation of the references to colour in this figure legend, the reader is referred to the web version of this article.)

an explicit means to approximate the best possible constraint for the nuisance field. We defined the threshold constraint ε to set the minimum nuisance current amplitude affecting the optimization process in L1L1 and L1L2, whereas in TLS, a weight is incorporated instead as a multiplier of the corresponding term in the objective function.

In the search case (A), which aimed at maximizing focused vs. nuisance field current ratio Θ, the method produced a focal current pattern and a well-localized stimulus current density during the first-stage with optimization threshold $\Gamma \geq 0.11$ A/m², adequate enough for an injecting current pattern of 4 mA [5,6]. This result is in accordance with our initial hypothesis on the potential
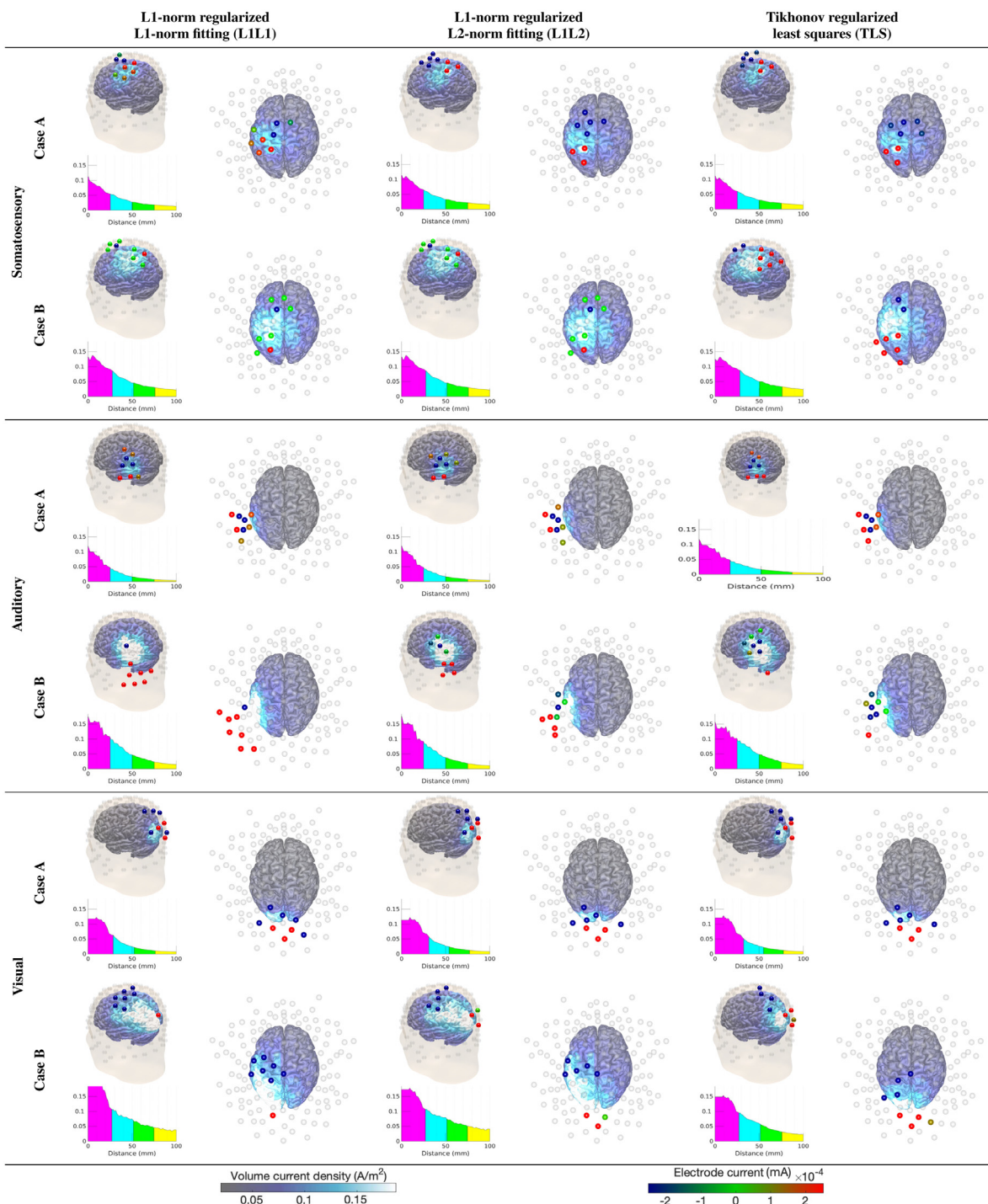
Fig. 6. The 8-channel electrode montage and current pattern (mA) together with corresponding volume current density A/m^2 were obtained through two consecutive runs of the two-stage metaheuristic optimization process concerning non-fixed and fixed montage of 8 active electrodes, respectively. Average amplitude in the direction of the target dipole is shown as a function of distance (mm) from the dipole position. The current pattern colorbar shows a color gradient interval from -0.25 to 0.25 mA to enhance the visibility of small variations in the pattern. (For interpretation of the references to colour in this figure legend, the reader is referred to the web version of this article.)

benefit in localizing the stimulus current and the general knowledge that L1-norm optimization is advantageous to enhance contrasts between different solution components [26,27].

In the search case (B), which concentrated on maximizing focused current density Γ, the L1L1 method produced the greatest compared to the L1L2 and TLS methods which is in agreement with earlier observations [22]. Maximizing Γ with an L1-norm data fit led to a two-patch montage following the extended reciprocity

principle [2]. Such a montage could effectively be found around the somatosensory area. However, the results for the auditory and visual areas were asymmetric, one polarity could be sharply distinguished by a single channel, while the opposite matches a cluster of channels instead, suggesting a potential numerical performance limitation of the applied solver algorithm.

Optimization performance are expected to behave differently case-wise by the applied lattice resolution into finding the thresh-

old weight ε. Namely, we found a focal solution within a regularization parameter α range approximately between -70 and -40 dB, where ε could be set down to -110 dB smaller than its surroundings without collapsing the amplitude of the candidate solution, related to the numerical accuracy of spatial discretization. For this reason, an enhanced lattice can improve the search accuracy with a slightly improved nuisance field suppression while maintaining an increasing amplitude in its vicinity. Achieving such an enhancement might be challenging if a hard upper-bound (e.g., [2,24]) suppressing the amplitude is applied instead of a threshold weight. For this reason, the constraint support (Section 2.1.1) is to be determined *a priori*, while in the present model is obtained *a posteriori* as a result of the optimization process.

The differences between the L1L1 and L1L2 methods were systematical, attributed to the mutual discrepancies in numerical performance as the formulations of these methods were similar when the nuisance field is not suppressed, i.e., when $\varepsilon = 1$ (Section 2.1.2). The parameters applied in the lattice search includes the neighborhoods of the global maximizers for Γ and Θ, and a 15×15 lattice grid which allowed finding a set of feasible solutions in a relatively short computing time (378, 456, and 20 s with L1L1, L1L2, and TLS, respectively). The former method implementation ran faster than the latter as it did not include additional quadratic constraints, which are necessary for a semi-definite formulation of a linearly constrained problem [38]. Furthermore, in addition to being a simple method, the TLS method was automatically parallelized by Matlab's interpreter, as it includes only full matrices and relatively simple linear algebraic operations, which explains the computing time differences compared to L1L1 and L1L2 optimization.

Potential future work would be to compare the present metaheuristic CVX/SDPT3-based L1L1 and L1L2 implementations with alternative interior-point techniques, simplex methods, or other convex strategies, e.g., the Alternating Direction Method of Multipliers (ADMM) [24,25]. Our optimizers, available in ZI [29], can be potentially expanded to include other brain stimulation modalities, for instance, Deep Brain Stimulation applications [50]. Further investigations of the relationship between the nuisance field threshold weight ε (tolerance) and modeling of other uncertainties is an important topic, as the latter aspect may be expected to limit maximal obtainable accuracy for this field. Finally, experimental work will be needed to learn more about other than mathematical or computational aspects of L1L1-optimized current patterns in practice.

Declaration of Competing Interest

The authors certify that this study is a result of purely academic, open, and independent research. They have no affiliations with or involvement in any organization or entity with a financial interest or non-financial interest such as personal or professional relationships, affiliations, knowledge, or beliefs in the subject matter or materials discussed in this manuscript.

Acknowledgments

Appendix A. Forward model

The governing partial differential equation for the electric potential in the head model Ω is of the form

$$\nabla \cdot (\sigma \nabla u) = 0. \tag{17}$$

The head model Ω is stimulated through an electrodes montage $(e_\ell)_{\ell=1}^L$ of size $|e_\ell|$. We denote the current applied on the ℓth electrode by $\mathbf{I}_\ell$, electrode potential $\mathbf{U}_\ell$, and impedance $\mathbf{Z}_\ell$. The boundary conditions for the Complete Electrode Model (CEM) are the following:

$$0 = \sigma \frac{\partial u}{\partial n}(\vec{r}), \qquad \text{for } \vec{r} \in \partial\Omega \setminus \cup_{\ell=1}^L e_\ell, \tag{18}$$

$$I_\ell = \int_{e_\ell} \sigma \frac{\partial u}{\partial n}(\vec{r}) dS, \qquad \text{for } \ell = 1, \dots, L, \tag{19}$$

$$U_\ell = u(\vec{r}) + \tilde{Z}_\ell \sigma \frac{\partial u}{\partial n}(\vec{r}), \qquad \text{for } \vec{r} \in e_\ell, \ \ell = 1, \dots, L. \tag{20}$$

The boundary condition 18 describes that no current is flowing inside nor outside of head; 19 describes that the total current flux through the ℓth electrode equals to the applied current I_ℓ; 20 describes the relationship between the ungrounded electrode potential U_ℓ and the potential u underneath the electrode; By assuming that the effective contact impedance is $\tilde{Z}_\ell = Z_\ell |e_\ell|$, we can rewrite 20 as

$$U_\ell = \frac{\int_{e_\ell} u \, dS}{|e_\ell|} + Z_\ell I_\ell. \tag{21}$$

A1. Weak form

A general weak form for electric potential field $u \in H^1(\Omega)$ can be obtained integrating by parts. Here, $H^1(\Omega)$ denotes a *Sobolev space* of square integrable ($\int_\Omega |u|^2 \, dV < \infty$) functions with square integrable partial derivatives. By multiplying 17 with a smooth enough test function $v \in S$, where S is a subspace of $H^1(\Omega)$, it follows that

$$\begin{aligned} 0 &= -\int_\Omega \nabla \cdot (\sigma \nabla u) v \, dV, \\ &= \int_\Omega \sigma \nabla u \cdot \nabla v \, dV - \int_{\partial\Omega} \sigma \frac{\partial u}{\partial n} v \, dS, \\ &= \int_\Omega \sigma \nabla u \cdot \nabla v \, dV - \sum_{\ell=1}^L \int_{e_\ell} \sigma \frac{\partial u}{\partial n} v \, dS. \end{aligned} \tag{22}$$

In addition, we have the following equations:

$$\begin{aligned} -\sum_{\ell=1}^L \int_{e_\ell} \sigma \frac{\partial u}{\partial n} v \, dS &= -\sum_{\ell=1}^L \frac{U_\ell}{Z_\ell |e_\ell|} \int_{e_\ell} v \, dS \\ &\quad + \sum_{\ell=1}^L \frac{1}{Z_\ell |e_\ell|} \int_{e_\ell} u v \, dS. \end{aligned} \tag{23}$$

As a result, we may rewrite the formula (*A*.6) as follows:

$$\begin{aligned} 0 &= \int_\Omega \sigma \nabla u \cdot \nabla v \, dV - \sum_{\ell=1}^L \frac{I_\ell}{|e_\ell|} \int_{e_\ell} v \, dS \\ &\quad - \sum_{\ell=1}^L \frac{1}{Z_\ell |e_\ell|^2} \int_{e_\ell} u \, dS \int_{e_\ell} v \, dS \\ &\quad + \sum_{\ell=1}^L \frac{1}{Z_\ell |e_\ell|} \int_{e_\ell} u v \, dS, \end{aligned} \tag{24}$$

for all $v \in S$. The left-side of 24 defines a *diffusion operator*. On the right-side, the first term corresponds to *neural activity*, the second term to the *targeted stimulus*, the third and fourth terms describe the *shunting effects*.

A2. Resistivity matrix

Given the scalar valued functions $\psi_1, \psi_2, \ldots, \psi_N \in \mathcal{S}$, the potential $\mathbf{u}$ can be approximated as the finite sum $\mathbf{u} = \sum_{i=1}^{N} z_i \psi_i$. Denoting by $\mathbf{z} = (z_1, z_2, \ldots, z_N)$ the coordinate vector of the discretized potential, by $\mathbf{w} = (w_1, w_2, \ldots, w_L)$ the (ungrounded) electrode voltages, and by $\mathbf{y} = (y_1, y_2, \ldots, y_L)$ as the injected current pattern, the weak form 24 is given by

$$
\begin{pmatrix} \mathbf{A} & -\mathbf{B} \\ -\mathbf{B}^T & \mathbf{C} \end{pmatrix} \begin{pmatrix} \mathbf{z} \\ \mathbf{w} \end{pmatrix} = \begin{pmatrix} \mathbf{0} \\ \mathbf{y} \end{pmatrix}. \tag{25}
$$

Here, $\mathbf{A}$ (N-by-N) is of the form

$$
a_{i,j} = \int_{\Omega} \sigma \nabla \psi_i \cdot \nabla \psi_j \, dV + \sum_{\ell=1}^{L} \frac{1}{Z_\ell |e_\ell|} \int_{e_\ell} \psi_i \psi_j \, dS, \tag{26}
$$

and the entries of $\mathbf{B}$ (N-by-L) and $\mathbf{C}$ (L-by-L) are given by

$$
b_{i,\ell} = \frac{1}{Z_\ell |e_\ell|} \int_{e_\ell} \psi_i \, dS, \tag{27}
$$

$$
c_{\ell,\ell} = \frac{1}{Z_\ell}. \tag{28}
$$

Consequently, the resistivity matrix $\mathbf{R}$ satisfying $\mathbf{z} = \mathbf{R}\mathbf{y}$ can be expressed as

$$
\mathbf{R} = \mathbf{A}^{-1}\mathbf{B}(\mathbf{C} - \mathbf{B}^T\mathbf{A}^{-1}\mathbf{B})^{-1}. \tag{29}
$$

The ungrounded electrode voltages $\mathbf{w}$ can be obtained by referring to the bottom row of 25, i.e., $\mathbf{y} = -\mathbf{B^T}\mathbf{z} + \mathbf{C}\mathbf{w}$.

A3. Lead field matrix

By $\mathbf{F}^{(k)}$ we denote a matrix which evaluates the kth Cartesian component of the volume current density $-\sigma \nabla u$ when multiplied by the coordinate vector $\mathbf{z}$ of the discretized electrical potential distribution $\mathbf{u}$. The entries of this matrix are given by

$$
f_{i,\ell}^{(k)} = \begin{cases} -(\sigma_{ij}(\nabla \psi_\ell)_j)^k, & \text{if } \operatorname{supp}\{\psi_\ell\} \cap T_i \neq \emptyset \\ 0, & \text{otherwise}, \end{cases} \tag{30}
$$

for $k = 1, 2, 3$ and $i, j, \ell = 1, 2, \ldots, N$ where subsets T_i, $i = 1, 2, \ldots, N$ form a partitioning of Ω for a user-defined dimension N. The kth Cartesian component of the discretized volume current distribution given the stimulating current pattern can be obtained as follows $\mathbf{F}^{(k)}\mathbf{R}\mathbf{y}$, where $\mathbf{F}^{(k)} = (f_{i,\ell}^{(k)})^T$, $k = 1, 2, 3$. Further, we define lead field matrix $\mathbf{L}$ as

$$
\mathbf{L} = \begin{pmatrix} \mathbf{F}^{(1)} \\ \mathbf{F}^{(2)} \\ \mathbf{F}^{(3)} \end{pmatrix} \mathbf{R} = \mathbf{F}\mathbf{R}, \tag{31}
$$

where $\mathbf{F} = (\mathbf{F}^{(1)}, \mathbf{F}^{(2)}, \mathbf{F}^{(3)})^T$ and $\mathbf{L} = (\mathbf{L}^{(1)}, \mathbf{L}^{(2)}, \mathbf{L}^{(3)})^T$ with components $\mathbf{L}^{(k)} = (\mathbf{L}_1^{(k)}, \mathbf{L}_2^{(k)})^T$, $k = 1, 2, 3$. Formula (31) can be considered as the *forward mapping* in the process of optimizing the current pattern.

Appendix B. The effect of weighting in TLS

Denoting $\mathbf{W} = (\mathbf{L}_1^T\mathbf{L}_1 + \alpha^2\sigma^2\mathbf{I})^{-1}$ and by $\tilde{\mathbf{y}} = \mathbf{W}\mathbf{L}_1^T\mathbf{x}_1$ the special solution of (12) with $\delta = 0$, the general solution of (12) can be written as

$$
\mathbf{y} = (\mathbf{I} + \delta^2\alpha^2\mathbf{W}\mathbf{L}_2^T\mathbf{L}_2)^{-1}\tilde{\mathbf{y}} = \tilde{\mathbf{y}} - \delta^2\alpha^2\mathbf{W}\mathbf{L}_2^T\mathbf{L}_2\tilde{\mathbf{y}}
$$
$$
+ O(\delta^4), \tag{32}
$$

following from the geometric series formula

$$
(\mathbf{I} + \delta^2\alpha^2\mathbf{W}\mathbf{L}_2^T\mathbf{L}_2)^{-1} = \mathbf{I} - \delta^2\alpha^2\mathbf{W}\mathbf{L}_2^T\mathbf{L}_2
$$
$$
+ \delta^4\alpha^4\mathbf{W}^2(\mathbf{L}_2^T\mathbf{L}_2)^2 - \cdots \tag{33}
$$

with assumption that $\delta < 1$, so that $\delta^2\alpha^2\|\mathbf{W}\mathbf{L}_2^T\mathbf{L}_2\|_2^2 \leq 1$. When $\delta = 0$, the special solution $\tilde{\mathbf{y}}$ gives the most intense current distribution to the direction of $\mathbf{x}$ at the targeted location, while the ratio between the focused field and nuisance field increases along with the value of $\delta \geq 0$. Namely, the inner product between the focused field and the targeted stimulus is of the form

$$
\mathbf{x}_1^T\mathbf{L}_1\mathbf{y} = \mathbf{x}_1^T\mathbf{L}_1\tilde{\mathbf{y}} - \delta^2\alpha^2\mathbf{x}_1^T\mathbf{L}_1\mathbf{W}\mathbf{L}_2^T\mathbf{L}_2\tilde{\mathbf{y}} + O(\delta^4)
$$
$$
= \mathbf{x}_1^T\mathbf{L}_1\tilde{\mathbf{y}} - \delta^2\alpha^2\tilde{\mathbf{y}}^T\mathbf{L}_2^T\mathbf{L}_2\tilde{\mathbf{y}} + O(\delta^4) \tag{34}
$$

which can be further written as the following ratio between Γ defined in (13) and $\tilde{\Gamma} = \frac{\mathbf{x}_1^T\mathbf{L}_1\tilde{\mathbf{y}}}{\|\mathbf{x}_1\|_2}$, respectively:

$$
\frac{\Gamma}{\tilde{\Gamma}} = \frac{\mathbf{x}_1^T\mathbf{L}_1\mathbf{y}}{\mathbf{x}_1^T\mathbf{L}_1\tilde{\mathbf{y}}} = 1 - \delta^2\alpha^2\frac{\|\mathbf{L}_2\tilde{\mathbf{y}}\|_2^2}{\mathbf{x}_1^T\mathbf{L}_1\tilde{\mathbf{y}}} + O(\delta^4). \tag{35}
$$

The squared norm of the nuisance field can be written as $\mathbf{L}_2\mathbf{y} = \mathbf{L}_2\tilde{\mathbf{y}} - \delta^2\alpha^2\mathbf{L}_2\mathbf{W}\mathbf{L}_2^T\mathbf{L}_2\tilde{\mathbf{y}} + O(\delta^4)$, which yields the ratio

$$
\frac{\|\mathbf{L}_2\mathbf{y}\|_2^2}{\|\mathbf{L}_2\tilde{\mathbf{y}}\|_2^2} = 1 - 2\,\delta^2\alpha^2\frac{\|\mathbf{L}_2^T\mathbf{L}_2\tilde{\mathbf{y}}\|_W^2}{\|\mathbf{L}_2\tilde{\mathbf{y}}\|_2^2} + O(\delta^4), \tag{36}
$$

where for convenience we have used the following norm definition $\|\mathbf{z}\|_W^2 := \mathbf{z}^T\mathbf{W}\mathbf{z}$. The square root of (36) is of the form

$$
\frac{\|\mathbf{L}_2\mathbf{y}\|_2}{\|\mathbf{L}_2\tilde{\mathbf{y}}\|_2} = 1 - \delta\alpha\frac{\|\mathbf{L}_2^T\mathbf{L}_2\tilde{\mathbf{y}}\|_W}{\|\mathbf{L}_2\tilde{\mathbf{y}}\|_2} + O(\delta^2), \tag{37}
$$

following from the Maclaurin series of the function $h(\tau) = (1 + \tau)^{1/2}$. Formulas (35) and (37) show that as $0 < \delta < 1$ increases, the focused field intensity decreases linearly, i.e., with a slower rate than the quadratically decreasing nuisance field norm. Hence the ratio Θ defined in (14) increases. The validity of the total dose and maximum current constraint is taken care of by scaling the solution after the minimization process in the respective order.

References

[1] C.S. Herrmann, S. Rach, T. Neuling, D. Strüber, Transcranial alternating current stimulation: a review of the underlying mechanisms and modulation of cognitive processes, Front. Hum. Neurosci. 7 (2013) 279.

[2] M. Fernandez-Corazza, S. Turovets, C.H. Muravchik, Unification of optimal targeting methods in transcranial electrical stimulation, Neuroimage 209 (2020) 116403.

[3] M.A. Nitsche, W. Paulus, Excitability changes induced in the human motor cortex by weak transcranial direct current stimulation, J. Physiol. 527 (3) (2000) 633–639, doi:10.1111/j.1469-7793.2000.t01-1-00633.x.

[4] A.V. Peterchev, T.A. Wagner, P.C. Miranda, M.A. Nitsche, W. Paulus, S.H. Lisanby, A. Pascual-Leone, M. Bikson, Fundamentals of transcranial electric and magnetic stimulation dose: definition, selection, and reporting practices, Brain. Stimul. 5 (4) (2012) 435–453, doi:10.1016/j.brs.2011.10.001.

[5] F. Fregni, P.S. Boggio, M. Nitsche, A. Pascual-Leone, Transcranial direct current stimulation, Br. J. Psychiatry 186 (5) (2005) 446–447, doi:10.1192/bjp.186.5.446.

[6] N. Khadka, H. Borges, B. Paneri, T. Kaufman, E. Nassis, A.L. Zannou, Y. Shin, H. Choi, S. Kim, K. Lee, M. Bikson, Adaptive current tDCS up to 4 mA, Brain Stimul. 13 (1) (2020) 69–79, doi:10.1016/j.brs.2019.07.027.

[7] I. Moreno-Duarte, N. Gebodh, P. Schestatsky, B. Guleyupoglu, D. Reato, M. Bikson, F. Fregni, Chapter 2 - transcranial electrical stimulation: transcranial direct current stimulation (tDCS), transcranial alternating current stimulation (tACS), transcranial pulsed current stimulation (tPCS), and transcranial random noise stimulation (tRNS), in: R. Cohen Kadosh (Ed.), The Stimulated Brain, Academic Press, San Diego, 2014, pp. 35–59, doi:10.1016/B978-0-12-404704-4.00002-8.

[8] A. Datta, J.M. Baker, M. Bikson, J. Fridriksson, Individualized model predicts brain current flow during transcranial direct-current stimulation treatment in responsive stroke patient, Brain Stimul. 4 (3) (2011) 169–174, doi:10.1016/j.brs.2010.11.001.

[9] T. Neuling, S. Wagner, C.H. Wolters, T. Zaehle, C.S. Herrmann, Finite-element model predicts current density distribution for clinical applications of tDCS and tACS, Front. Psychiatry 3 (2012) 83.

[10] R. Lindenberg, V. Renga, L. Zhu, D. Nair, G. Schlaug, Bihemispheric brain stimulation facilitates motor recovery in chronic stroke patients, Neurology 75 (24) (2010) 2176–2184, doi:10.1212/WNL.0b013e318202013a.

[11] F. Fregni, S. Thome-Souza, M.A. Nitsche, S.D. Freedman, K.D. Valente, A. Pascual-Leone, A controlled clinical trial of cathodal DC polarization in patients with refractory epilepsy, Epilepsia 47 (2) (2006) 335–342, doi:10.1111/j.1528-1167.2006.00426.x.

[12] P.S. Boggio, R. Ferrucci, S.P. Rigonatti, P. Covre, M. Nitsche, A. Pascual-Leone, F. Fregni, Effects of transcranial direct current stimulation on working memory in patients with Parkinson's disease, J. Neurol. Sci. 249 (1) (2006) 31–38, doi:10.1016/j.jns.2006.05.062. Terrorism for the Neurologist

[13] D.H. Benninger, M. Lomarev, G. Lopez, E.M. Wassermann, X. Li, E. Considine, M. Hallett, Transcranial direct current stimulation for the treatment of Parkinson's disease, J. Neurol. Neurosur. Psychiatry 81 (10) (2010) 1105–1111, doi:10.1136/jnnp.2009.202556.

[14] F. Fregni, D.K. Simon, A. Wu, A. Pascual-Leone, Non-invasive brain stimulation for Parkinson's disease: a systematic review and meta-analysis of the literature, J. Neurol. Neurosurg. Psychiatry 76 (12) (2005) 1614–1623, doi:10.1136/jnnp.2005.069849.

[15] F. Fregni, P.S. Boggio, M.C. Santos, M. Lima, A.L. Vieira, S.P. Rigonatti, M.T.A. Silva, E.R. Barbosa, M.A. Nitsche, A. Pascual-Leone, Noninvasive cortical stimulation with transcranial direct current stimulation in Parkinson's disease, Movement Disorders 21 (10) (2006) 1693–1702, doi:10.1002/mds.21012.

[16] P.S. Boggio, F. Bermpohl, A.O. Vergara, A.L. Muniz, F.H. Nahas, P.B. Leme, S.P. Rigonatti, F. Fregni, Go-no-go task performance improvement after anodal transcranial DC stimulation of the left dorsolateral prefrontal cortex in major depression, J. Affect. Disord. 101 (1) (2007) 91–98, doi:10.1016/j.jad.2006.10.026.

[17] F. Fregni, P.S. Boggio, M.A. Nitsche, M.A. Marcolin, S.P. Rigonatti, A. Pascual-Leone, Treatment of major depression with transcranial direct current stimulation, Bipolar Disord. 8 (2) (2006) 203–204, doi:10.1111/j.1399-5618.2006.00291.x.

[18] M.A. Nitsche, P.S. Boggio, F. Fregni, A. Pascual-Leone, Treatment of depression with transcranial direct current stimulation (tDCS): a review, Exp. Neurol. 219 (1) (2009) 14–19, doi:10.1016/j.expneurol.2009.03.038. Brain Stimulation in Psychiatry

[19] F. Fregni, R. Gimenes, A.C. Valle, M.J.L. Ferreira, R.R. Rocha, L. Natalle, R. Bravo, S.P. Rigonatti, S.D. Freedman, M.A. Nitsche, A. Pascual-Leone, P.S. Boggio, A randomized, sham-controlled, proof of principle study of transcranial direct current stimulation for the treatment of pain in fibromyalgia, Arthritis Rheumatism 54 (12) (2006) 3988–3998, doi:10.1002/art.22195.

[20] A. Antal, T.Z. Kincses, M.A. Nitsche, W. Paulus, Manipulation of phosphene thresholds by transcranial direct current stimulation in man, Exp. Brain Res. 150 (3) (2003) 375–378, doi:10.1007/s00221-003-1459-8.

[21] P.S. Boggio, N. Sultani, S. Fecteau, L. Merabet, T. Mecca, A. Pascual-Leone, A. Basaglia, F. Fregni, Prefrontal cortex modulation using transcranial dc stimulation reduces alcohol craving: a double-blind, sham-controlled study, Drug Alcohol. Depend. 92 (1) (2008) 55–60, doi:10.1016/j.drugalcdep.2007.06.011.

[22] J.P. Dmochowski, A. Datta, M. Bikson, Y. Su, L.C. Parra, Optimized multi-electrode stimulation increases focality and intensity at target, J. Neural Eng. 8 (4) (2011) 046011.

[23] J.P. Dmochowski, L. Koessler, A.M. Norcia, M. Bikson, L.C. Parra, Optimal use of eeg recordings to target active brain areas with transcranial electrical stimulation, Neuroimage 157 (2017) 69–80.

[24] S. Wagner, M. Burger, C.H. Wolters, An optimization approach for well-targeted transcranial direct current stimulation, SIAM J. Appl. Math. 76 (6) (2016) 2154–2174.

[25] A. Khan, M. Antonakakis, N. Vogenauer, J. Haueisen, C.H. Wolters, Individually optimized multi-channel tDCS for targeting somatosensory cortex, Clin. Neurophysiol. 134 (2022) 9–26.

[26] J. Kaipio, E. Somersalo, Statistical and Computational Inverse Problems, vol. 160, Springer Science & Business Media, 2006.

[27] M. Bertero, P. Boccacci, Introduction to Inverse Problems in Imaging, CRC press, 2020.

[28] M. Grant, S. Boyd, Y. Ye, Cvx users' guide, in: Tech. Rep. Build, Cambridge Univ., 2009, p. 711.

[29] Q. He, A. Rezaei, S. Pursiainen, Zeffiro user interface for electromagnetic brain imaging: a GPU accelerated FEM tool for forward and inverse computations in Matlab, Neuroinformatics (2019) 1–14.

[30] A. Rezaei, J. Lahtinen, F. Neugebauer, M. Antonakakis, M.C. Piastra, A. Koulouri, C.H. Wolters, S. Pursiainen, Reconstructing subcortical and cortical somatosensory activity via the RAMUS inverse source analysis technique using median nerve SEP data, Neuroimage 245 (2021) 118726.

[31] T. Miinalainen, A. Rezaei, D. Us, A. Nüßing, C. Engwer, C.H. Wolters, S. Pursiainen, A realistic, accurate and fast source modeling approach for the eeg forward problem, Neuroimage 184 (2019) 56–67.

[32] S. Pursiainen, F. Lucka, C.H. Wolters, Complete electrode model in EEG: relationship and differences to the point electrode model, Phys. Med. Biol. 57 (4) (2012) 999–1017.

[33] S. Pursiainen, B. Agsten, S. Wagner, C.H. Wolters, Advanced boundary electrode modeling for tES and parallel tES/EEG, IEEE Trans. Neural Syst. Rehabil. Eng. 26 (1) (2017) 37–44.

[34] T. Kowalski, J. Silny, H. Buchner, Current density threshold for the stimulation of neurons in the motor cortex area, Bioelectromagnetics 23 (6) (2002) 421–428.

[35] S. Murakami, Y. Okada, Invariance in current dipole moment density across brain structures and species: physiological constraint for neuroimaging, Neuroimage 111 (2015) 49–58, doi:10.1016/j.neuroimage.2015.02.003.

[36] S. Murakami, T. Zhang, A. Hirose, Y.C. Okada, Physiological origins of evoked magnetic fields and extracellular field potentials produced by guinea-pig CA3 hippocampal slices, J. Physiol. 544 (1) (2002) 237–251.

[37] S. Boyd, L. Vandenberghe, Convex Optimization, Cambridge University Press, 2004. https://books.google.fi/books?id=IUZdAAAAQBAJ

[38] R.H. Tütüncü, K.-C. Toh, M.J. Todd, Solving semidefinite-quadratic-linear programs using SDPT3, Math. Program. 95 (2) (2003) 189–217.

[39] F. Glover, K. Sörensen, Metaheuristics, Scholarpedia 10 (4) (2015) 6532.

[40] A. Roy, E. Boroda, E. Waldron, K. Lim, T. Henry, Integration of prefrontal transcranial direct current stimulation with cognitive training for treatment of memory dysfunction in epilepsy, Brain Stimul. 12 (2) (2019) 481.

[41] A. Tost, C. Migliorelli, A. Bachiller, I. Medina-Rivera, S. Romero, Á. García-Cazorla, M.A. Mañanas, Choosing strategies to deal with artifactual EEG data in children with cognitive impairment, Entropy 23 (8) (2021) 1030.

[42] K. Brodmann, Brodmann's: Localisation in the Cerebral Cortex, Springer Science & Business Media, 2007.

[43] O.D. Creutzfeldt, G.H. Fromm, H. Kapp, Influence of transcortical dc currents on cortical neuronal activity, Exp. Neurol. 5 (6) (1962) 436–452.

[44] J. Malmivuo, V. Suihko, H. Eskola, Sensitivity distributions of eeg and meg measurements, IEEE Trans. Biomed. Eng. 44 (1997) 196–208, doi:10.1109/10.554766.

[45] M. Rullmann, A. Anwander, M. Dannhauer, S.K. Warfield, F.H. Duffy, C.H. Wolters, Eeg source analysis of epileptiform activity using a 1 mm anisotropic hexahedra finite element head model, Neuroimage 44 (2) (2009) 399–410.

[46] V. Montes-Restrepo, P. Van Mierlo, G. Strobbe, S. Staelens, S. Vandenberghe, H. Hallez, Influence of skull modeling approaches on eeg source localization, Brain Topogr. 27 (2014) 95–111, doi:10.1007/s10548-013-0313-y.

[47] M. Dannhauer, B. Lanfer, C.H. Wolters, T.R. Knösche, Modeling of the human skull in EEG source analysis, Hum. Brain Mapp. 32 (9) (2011) 1383–1399, doi:10.1002/hbm.21114.

[48] V. Jurcak, D. Tsuzuki, I. Dan, 10/20, 10/10, and 10/5 systems revisited: their validity as relative head-surface-based positioning systems, Neuroimage 34 (4) (2007) 1600–1611, doi:10.1016/j.neuroimage.2006.09.024.

[49] T. Sauer, Numerical Analysis, Pearson, 2018. https://books.google.fi/books?id=2rKgtAEACAAJ

[50] S. Järvenpää, Optimization of deep brain stimulation of the anterior nucleus of thalamus for refractory epilepsy, Tampere University, 2020 Ph.D. thesis.